Mechanisms of soot-aggregate restructuring and compaction

Joel C. Corbin[1,2]**, Robin L. Modini**[1]**, and Martin Gysel-Beer**[1]

[1]Laboratory of Atmospheric Chemistry, Paul Scherrer Institute, 5232 Villigen, Switzerland
[2]Now at: Metrology Research Centre, National Research Council Canada, 1200 Montreal Rd, Ottawa, Canada

Correspondence to: Joel.Corbin@nrc-cnrc.gc.ca

Abstract.

Soot aggregates form as open, fractal-like structures, but aged atmospheric particles are often observed to be restructured into more-compact shapes due to internal mixing ("coating"). This compaction has a major effect on the radiative properties of the aggregates, and may also influence their aerosol-cloud interactions, toxicity, and deposition in human lungs. Recent laboratory studies have presented conflicting arguments on whether this compaction occurs during condensation or during the evaporation of coatings. In this three-part study, we combine theory and experiments to explain these conflicting results. First, we review the surface-science literature and identify explicit mechanisms for condensation-compaction as well as evaporation-compaction. We also identify a mechanism for *avoiding* compaction during condensation, based on heterogeneous nucleation theory and the kinetic barriers to capillary formation. Second, we review the soot-restructuring literature and find clear evidence for both condensation- and evaporation-compaction, with condensation-compaction being the norm. Third, we present new experimental results where the capillary forces due to anthracene coatings were "switched on" or "switched off" by using solid or liquid phases during coating addition and removal. Consequently, we demonstrate condensation-compaction, evaporation-compaction, and no compaction, for the same soot source. Overall, our study indicates that soot particles will typically undergo compaction when internal mixing occurs by the condensation of liquid coatings, while compaction may be avoided when internal mixing occurs through coagulation or the gas-to-particle formation of solid or highly viscous coatings.

Supporting information for

"Experimental compaction of soot aggregates by coating condensation and evaporation"

by Joel C. Corbin, Robin L. Modini, and Martin Gysel-Beer.

This Supplement contains additional discussion and figures related to the article.

S1 Mobility diameter and shape factor

The mobility diameter d_{mob} is given by (DeCarlo *et al.*, 2004),

$$\frac{d_{\mathrm{mob}}}{C_c(\mathrm{Kn}, d_{\mathrm{mob}})} = \chi(\mathrm{Kn})\frac{d_e}{C_c(\mathrm{Kn}, d_e)} \tag{S1}$$

where the dynamic shape factor $\chi(\mathrm{Kn})$ represents the ratio of the drag force on the particle to the drag force on its volume-equivalent sphere with diameter d_e, which is commonly obtained from single-particle mass (m_p) measurements via

$$m_p = \rho_p \frac{\pi}{6} d_e^3 \tag{S2}$$

when the particle material density ρ_p is known (DeCarlo *et al.*, 2004). In Equation S1, the function $C_c(\mathrm{Kn}, d)$ is the Cunningham slip correction, which accounts for the non-continuous nature of the gas-phase and which depends on the Knudsen number. In calculating the Cunningham slip correction C_c, we used the mean free path in air of 66.35 nm given by Jennings (1988). $\chi(\mathrm{Kn})$ is a function of the Knudsen number ($\mathrm{Kn} = 2\lambda/d$, where λ is the molecular mean free path of air and d is a particle diameter). For simplicity, we generally write χ for the transition-regime shape factor.

S2 Calculation of the phase diagram of anthracene

The phase diagram of anthracene was plotted using the Clausius-Clapeyron equation (Roux *et al.*, 2008),

$$\ln\frac{p_1}{p_2} = \frac{\Delta_x H}{R}\left(\frac{1}{T_2} - \frac{1}{T_1}\right) \tag{S3}$$

where $\Delta_x H$ was either the enthalpy of vapourization $\Delta_{vap}H$ or sublimation $\Delta_{sub}H$. These were taken as 79.9 kJ/mol and 101.9 kJ/mol, respectively, following Roux *et al.* (2008). Note that $\Delta_{sub}H$ is equal to the sum of $\Delta_{melting}H$ and $\Delta_{vap}H$. Finally, R is the ideal gas constant.

The Clausius-Clapeyron equation requires knowledge of a reference vapour pressure, which we obtained using the Antoine equation $log_{10}p = A - (B/(T+C))$, where p is the vapour pressure in bar at temperature T in Kelvin. We used $\{A, B, C\} = \{4.72997, 2759.53, -30.753\}$ from Burgess (2020) to estimate anthracene's vapour pressure at the bulk melting point of 489 K (216 °C). We then extrapolated this vapour pressure across the desired temperature range using the Clausius-Clapeyron equation and plotted the ratios of the calculated p. Though these coefficients are valid only down to 496.4 K (Burgess, 2020), our approach ensured overlap of the vapour pressures at the melting point. We did not find any literature values of p which resulted in a correct prediction of the melting point, which we attributed to the experimental difficulty in measuring the extremely low vapour pressures of solid anthracene (Roux *et al.*, 2008).

Reference: Donald R. Burgess, Jr. "Thermochemical Data" in NIST Chemistry WebBook, NIST Standard Reference Database Number 69, Eds. P.J. Linstrom and W.G. Mallard, National Institute of Standards and Technology, Gaithersburg MD, 20899, https://doi.org/10.18434/T4D303, (retrieved October 29, 2020).

S2.1   Phase diagram for designing restructuring experiments

Our anthracene experiments were designed based on the phase diagram shown in Figure S1a. The figure plots $S = p/p_0$, the saturation ratio with respect to liquid anthracene (Section **??**), against temperature. By definition, $S = 1$ for bulk liquid anthracene, while $S < 1$ for capillary liquids due to their curvature. The figure illustrates capillary curvature for equivalent diameters of curvature $> 2\,$nm (Ferry *et al.*, 2002). For solid anthracene, which exists only below the bulk melting point $T_{\mathrm{melt,\,bulk}}$, $S < 1$ due to the greater order of the solid phase. $T_{\mathrm{melt,\,bulk}}$ is illustrated by the vertical line at $488\,$K.

The anthracene phase diagram also includes a second vertical line to illustrate the melting point of nanoscale amounts of anthracene. This melting point, $T_{\mathrm{melt,\,p}}$, is substantially lower than $T_{\mathrm{melt,\,bulk}}$ due to the well-understood effects of melting-point depression (Pawlow, 1909; Schmidt *et al.*, 1998; Nanda, 2009; Christenson, 2001) which have even been specifically demonstrated in the context of soot compaction (Chen *et al.*, 2016).

The magnitude of nanoscale melting-point depression is quantified by the material constant β, which has been calculated as 1.303 for anthracene using molecular dynamics simulations (Chen *et al.*, 2014). The results of this prediction are shown by the upper axis of Figure S1a, which shows the size of a spherical particle with a melting point equal to the lower axis, $T_{\mathrm{melt,\,p}}$. The melting point function $T_{\mathrm{melt}}(m_p)$ increases asymptotically towards the bulk melting point $(215\,^{\circ}\mathrm{C})$ with particle size. Particles with d_e greater than about $100\,$nm diameter have $T_{\mathrm{melt}}(m_p)$ close to the bulk value, while small particles have much lower $T_{\mathrm{melt}}(m_p)$ For example, $T_{\mathrm{melt,\,p}} = 2\,$nm is found at $348\,$K $(75\,^{\circ}\mathrm{C})$, about 29% lower than the bulk melting point of $T_{\mathrm{melt,\,bulk}} = 488\,$K $(215\,^{\circ}\mathrm{C})$. These values should be taken as qualitative, as the calculated $T_{\mathrm{melt,\,p}}$ represents the equilibrium melting point; solids in confinement may remain liquid at even higher temperatures (Christenson, 2001). For example, Lopatkin *et al.* (1977) observed that anthracene films of thickness $10\,$nm to $16\,\mu$m form as liquids below $328\,$K. Nevertheless, these temperatures are comparable to our heater temperatures of 428–483 K, while some earlier work used lower temperatures (see Figures S7 and **??**, and Section **??**). Further details of $T_{\mathrm{melt}}(m_p)$ and its calculation are given in Figure S7 and Section S4.

Figure S1b illustrates the use of this phase diagram to design the soot compaction experiments in Section **??**. Each arc illustrates a process which we verified experimentally, primarily by measuring shape factors χ (Equation S1) as discussed below. The arcs illustrate capillary condensation at a single S (single pore size) for simplicity; in reality capillary adsorption would resemble an isotherm (e.g. Ferry *et al.*, 2002), though with relatively less adsorption than normal, since our experiments involved short timescales and therefore allowed less time for capillary condensation, t_c (Section **??**). Note that, for simplicity, the arcs on Figure S1 do not emphasize the potential influence of freezing within capillary pores (Marcolli, 2014), which may lower S above the particle after freezing.

Each of the phase changes in Figure S1 may be experimentally achieved as follows. Liquid condensation or solid deposition may be achieved by passing soot particles through a heated reservoir of a given coating material, followed by a cooling section. The cooling section will produce a profile of supersaturation that is dependent on the temperature profile across the heated and cooling sections, which depends on flow rate, tubing material, and tubing insulation (Nguyen *et al.*, 1987). The rate of increase of supersaturation will dictate the amount of time available for heterogeneous nucleation of vapours onto the particles (discussed in Section **??**). The maximum attained supersaturation will dictate the amount of coating condensed onto the sample particles. Condensation may occur via one of two processes, depending on the soot–coating contact angle θ and the supersaturation reached: it may form either menisci (first step of CC in Figure **??**) or beads (first step of NDA in Figure **??**) on the soot surface (Section **??**). Competitive condensation to the walls of the system will also occur (Nguyen *et al.*, 1987).

Evaporation may be achieved by decreasing the saturation ratio of the aerosol. This may be achieved by removing vapours and is dramatically accelerated at elevated temperatures. For oleic acid coatings, where the melting point is above room temperature, evaporation is trivial and can be achieved with a catalytic stripper or thermodenuder. For anthracene coatings, the melting point is well above room temperature even after taking melting-point depression into account. Evaporation requires heating the anthracene coating above its melting point $(\geq 80\,^{\circ}\mathrm{C})$ without allowing the coating to sublimate. We achieved this by passing anthracene-coated soot through our second coating apparatus, while the second apparatus was heated to high temperatures and also filled with anthracene. The sample then follows the evaporation curve in Figure S1 (thin blue solid line). Our apparatus was only able to sustain these conditions for a short period, before the anthracene in apparatus 2 was 'distilled' from the heating section to the cooler tubing downstream by sublimation-deposition.

When the second apparatus was depleted of anthracene, the sample followed the sublimation curve in Figure S1 (thin red line). Sublimation was also achieved by heating anthracene in the catalytic stripper and thermodenuder.

Thus, by combining the experimental conditions required to achieve each phase change, the four restructuring pathways in Table **??** may be achieved. To summarize, we achieved Path **LL** using oleic acid, and Paths **LS**, **SS**, and **SL** using anthracene. We achieved Path **LL** under

conditions where capillary condensation was possible, but not under conditions where NDA was possible (Figure **??**). The NDA mechanism has been achieved previously by others ((Ma *et al.*, 2013; Chen *et al.*, 2018)) as discussed in Section **??**.

S3 Additional Experimental Methods

S3.1 Soot samples

Soot was generated by a miniCAST 5201c soot generator (Jing Ltd., Switzerland) which consists of a partially-quenched propane diffusion flame. The miniCAST was operated under lean combustion combustions, with the following settings for each {gas, flow in mL min^{-1}}: {propane, 60}, {premixed nitrogen, 0}, {combustion air, 1550}, {dilution air, 2e4}. Premixed nitrogen refers to potential premixing with combustion air. We avoid using the CAST burner to produce so-called "low-BC fraction" soot, which is quenched earlier in the combustion process to produce incompletely-graphitized particles that are poor surrogates for atmospheric soot (Maricq, 2014). A 1.5 m^3 steel tank was used as a reservoir during the experiments.

S3.2 Real-time measurements

As depicted in Figure S2, a number of instruments were used to characterize the soot samples in real time. The total flow was 0.71 min^{-1}. A first Differential Mobility Analyzer (DMA1, built at PSI, with similar dimensions to the Model 3801 DMA of TSI Inc., USA) pre-selected particles, typically at 300 nm. The resulting monodisperse aerosol was either sampled directly or processed as described below.

The aerosol was measured by a Scanning Mobility Particle Sizer (SMPS; comprised of a similar DMA, DMA2, plus a TSI 3022a Condensation Particle Counter, CPC), scanning from 100 to 700 nm. In some cases, we bypassed DMA2 in order to test whether new particles (with diameter <100 nm) were forming in the coating apparatus; such conditions were always avoided. In parallel, a Single Particle Soot Photometer (SP2; Schwarz *et al.*, 2006; Laborde *et al.*, 2012) simultaneously measured single-particle BC mass m_{BC} by laser-induced incandescence and optical size by light scattering. The SP2 was frequently operated behind an Aerosol Particle Mass analyzer (APM; Model 3601, Kanomax Japan), which classifies particles by their mass-to-charge ratio m/q. Using custom software written in LabView, the APM was scanned through m/q settings while the SP2 was used to selectively count singly charged $(q = 1)$ BC particles exiting the APM. Like a high-resolution optical particle counter, the SP2 is able to discriminate singly charged particles because its signals are proportional to particle mass, which reduces ambiguity in the data relative to APM-CPC measurements. The modes of the resulting mass distributions were fitted by lognormal or asymmetric normal curves (Tajima *et al.*, 2011) and used to define the total particle mass. The measured total mass was used to calculate coating volumes as described in the manuscript.

S3.3 Offline measurements

TEM was performed with a JEOL 2010 at 200 keV after electrophoretic sampling particles onto 300-mesh copper grids with a 1-2 nm amorphous carbon film. The copper grids were obtained from Quantifoil (Großlöbichau, Germany).

Sampling was performed using a Partector (Naneos GmbH, Windisch, Switzerland), which charges particles with a corona charger before electrophoretic sampling. TEM samples were performed for the maximum coating volumes (maximum V_1/V_0).

S3.4 Soot coating addition and removal

Soot coatings were added using one of two apparatuses. The first was similar to that described by Moteki and Kondo (2007) and was constructed at PSI by M. Heringa. It consisted of two concentric stainless steel tubes (12 mm and 8 mm). Aerosol samples flowed in through the outer tube and out through the inner tube. The outer tube was terminated at one end by a stainless steel cap, which was filled with either oleic acid or anthracene crystals. The cap was placed on a hot plate and heated to saturate the aerosol flow. The second apparatus consisted of a simple copper tube wrapped first in heating tape, then in ice–water packs and was similar to that described by (Nguyen *et al.*, 1987). Coating materials were placed in a bend in the copper tube. The second apparatus was able to reach higher coating thicknesses due to the active cooling stage and the high thermal conductivity of copper. The second apparatus was also necessary for the anthracene evaporation experiments described in Section **??**.

The coating apparatuses were operated at different temperatures for oleic acid (90 %, Sigma-Aldrich) and anthracene (99 %, Sigma-Aldrich). For oleic acid condensation, the heater was operated between 94 and 140 °C. Above 140 °C new-particle formation occurred, indicating

that excessive supersaturations were being reached after the coating apparatus. Anthracene coatings were obtained with a heater temperature of $95-202\,^\circ$C. Above $202\,^\circ$C, the reservoir emptied too quickly for the measurements. Note that the thermocouple was placed between the heating plate and the sample, so the reported temperatures are upper limits. The lower half of the apparatus was insulated and the upper half cooled by room air to maximize the achieved supersaturations. For some anthracene experiments, even higher supersaturations were achieved by immersing the lower third of the apparatus in oil. The oleic acid experiments lasted one day and were performed in sequence: the highest temperatures were used last. Afterwards, the oleic acid was observed to have transformed from a light-yellow to a reddish-brown liquid, indicating that a chemical transformation had taken place. However, our results are consistent with previous work (Ghazi and Olfert, 2013) and indicate that this change had a negligible effect on the density of the oleic acid which was taken as $895\,\mathrm{kg\,m^3}$ in our calculations.

The anthracene experiments lasted three days in total and were not performed in sequence. The maximum temperature used was $202\,^\circ$C. In the early minutes of some high-temperature anthracene experiments, the SMPS appeared to measure the tail of a nucleation mode. As no difference in the results was observed when this mode was present, we conclude that it did not influence the experiments.

The primary denuder used in this work was a catalytic stripper (CS015, Catalytic Instruments GmbH, Rosenheim, Germany), which vapourizes and then oxidizes organic molecules at $350\,^\circ$C. In some experiments, this stripper was replaced with the activated-charcoal thermodenuder described by Burtscher *et al.* (2001), so that the additional experiments where soot was pre-denuded prior to coating could be performed. In those experiments, described in Section 4.2.3 in the manuscript, we pre-denuded soot at $350\,^\circ$C using the thermodenuder before coating particles as usual and denuding particles with the catalytic stripper, at $350\,^\circ$C to $200\,^\circ$C and $150\,^\circ$C. For all stripper temperatures, the original particle mass (mean $\pm$ standard deviation 6.40 ± 0.15 fg) was measured as returning to its original value, within uncertainty (6.38 ± 0.18 fg).

S4 Melting-point depression: further discussion and calculations

Physically, melting point depression may be alternatively viewed a reduction of intermolecular forces due to the disorder of nanoscopic quantities of anthracene (Aubin and Abbatt, 2006) or as the result of balancing bulk and surface energy terms (Christenson, 2001). The magnitude of melting-point depression for anthracene was estimated for Figure S7 using a size-dependent thermodynamic model of nanoscopic melting-point depression (Nanda, 2009):

$$\frac{T_{m,\,\mathrm{particle}}}{T_{m,\,\mathrm{bulk}}} = 1 - \left(\frac{\beta}{d_e}\right) \tag{S4}$$

where $T_{m,\,\mathrm{particle}}$ is the melting point of a particle with spherical-equivalent diameter d_e and $T_{m,\,\mathrm{bulk}}$ is the melting point of bulk material ($d_e >$ 100 nm, see Figure S7). This model has been validated experimentally (Nanda, 2009) and is valid for materials which melt homogeneously or from the surface inwards. Using a molecular-dynamics model, Chen *et al.* (2014) found that pyrene melts via both of these mechanisms (Chen *et al.*, 2014) and estimated the material-specific parameter β as 1.303 for pyrene (four compact aromatic rings) and 1.312 for coronene (seven compact rings). As these two values are virtually identical we have used $1.3 \pm 25\%$ for anthracene (three linear rings) in Figure S7. This β results in a melting point for 1 nm spheres which is about 2/3 of the melting point of bulk anthracene, which is close to the melting point depression measured experimentally by Lopatkin *et al.* (1977) for anthracene thin films. This consistency is in line with expectations, since β is a thermodynamic parameter, a function of the solid density, liquid density, surface energies of the solid–vapour and liquid–vapour interfaces, and the bulk latent heat of fusion (Nanda, 2009).

We note that our use of Equation S4 is different to that of Chen *et al.* (2016), who were the first to consider the effects of melting-point depression on soot restructuring. Those authors considered thin-film thicknesses when applying Equation S4, whereas we have considered equivalent spheres ($d_{\mathrm{sph\text{-}equiv}}$). They observed PAH restructuring at equivalent film thicknesses (calculated from single-particle mass measurements) of 0.2 nm, which is half the 0.4 nm thickness of a graphene sheet (Nemes-Incze *et al.*, 2008). They therefore argued that their observations demonstrated capillary condensation and restructuring, in agreement with the conclusions of the present work..
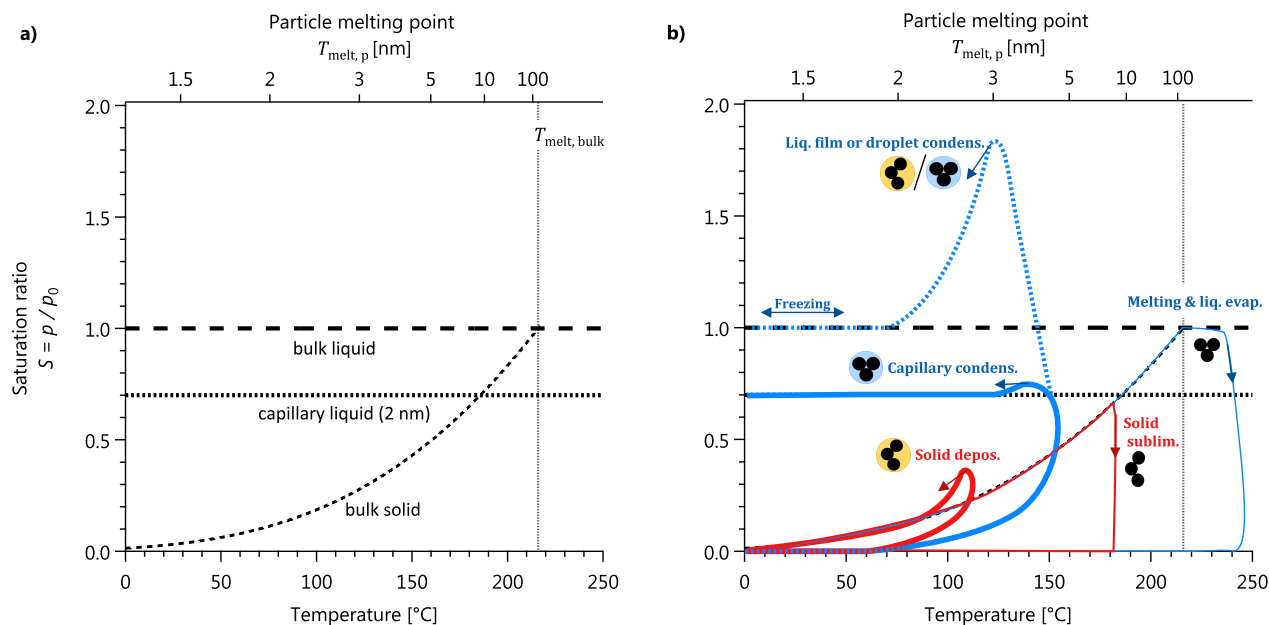
Figure S1. Equilibrium phase diagram for anthracene, as used to design the experiments shown in Figure **??**. Saturation ratios are plotted with respect to the bulk liquid vapour pressure, p_0. Panel **a** shows the equilibrium saturation ratios S for bulk solids, bulk liquids, capillary liquids with $> 2\,\text{nm}$ equivalent diameters and the melting-point depression associated with nanoscopic quantities of material (Section S2.1). Nanoscopic quantities of material are expressed in equivalent nanoparticle diameters on the top axes. Panel **b** qualitatively illustrates the experimental pathways used to add (thick lines) or remove (thin lines) coatings. Coatings are either solid (red) or liquid (blue) phase at the time of removal; line thicknesses are varied so that the different pathways can be distinguished visually. By combining one addition and one removal pathway, different compaction endpoints can be achieved, as shown by the particles. Note that the depicted maximum supersaturations are conservative; some laboratory studies have used $S > 20$.
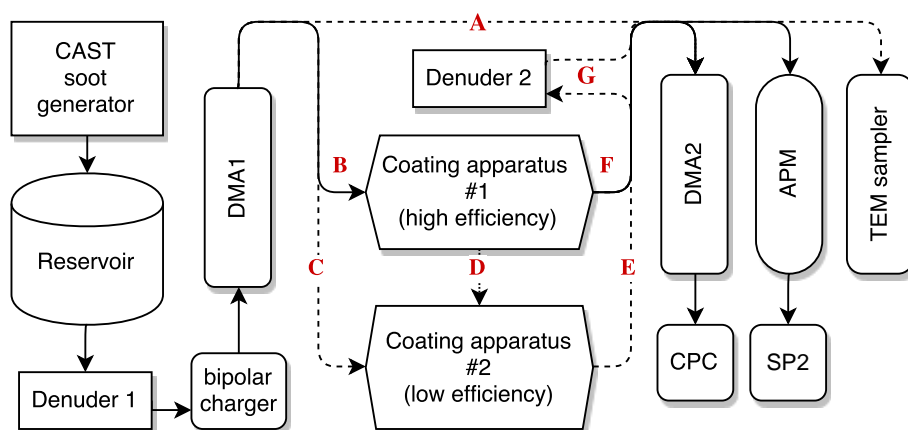

Figure S2. Experimental setup used to process soot particles through the different pathways given in Table **??** and related Figure **??**. Details of the coating apparatuses are illustrated in Figure S3. Pathways were achieved as follows. Path (**LL**): route **CEG** with oleic acid; Path (**LS**): route **CEG** with anthracene; Path (**SS**): route **BFG** with anthracene; Path (**SL**): route **BDE** with anthracene and anthracene-saturated walls in the second coating apparatus. Reference untreated samples were measured through line **A**. The denuder **G** was removed to measure coated particles. Dashed lines indicate temporary connections. The SP2 was used to differentiate particle charges only, not to measure single-particle mass.

S5   Supplementary figures
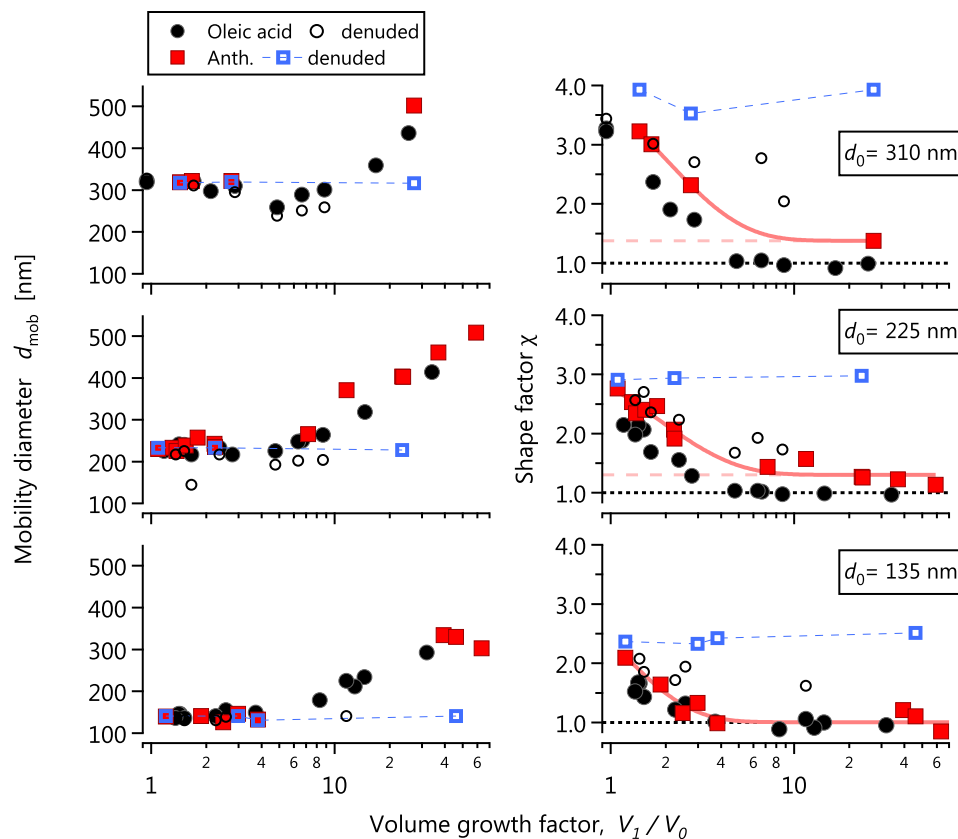
Coating apparatus #1
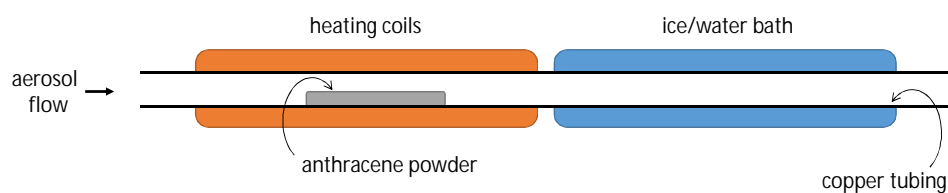
Coating apparatus #2
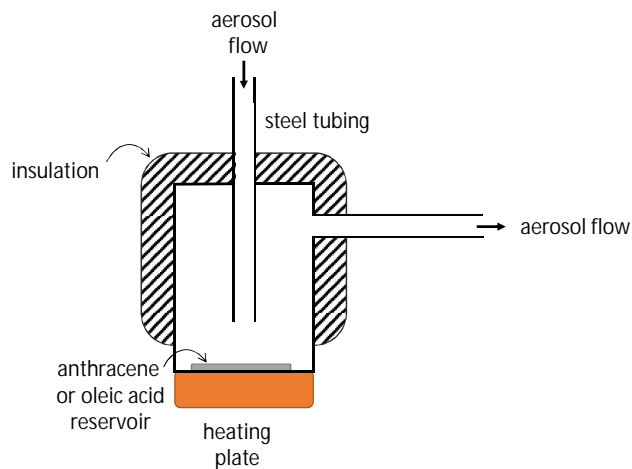
Figure S3. Schematic of the (a) high-efficiency copper coating apparatus #1 and (b) low-efficiency steel coating apparatus #2.
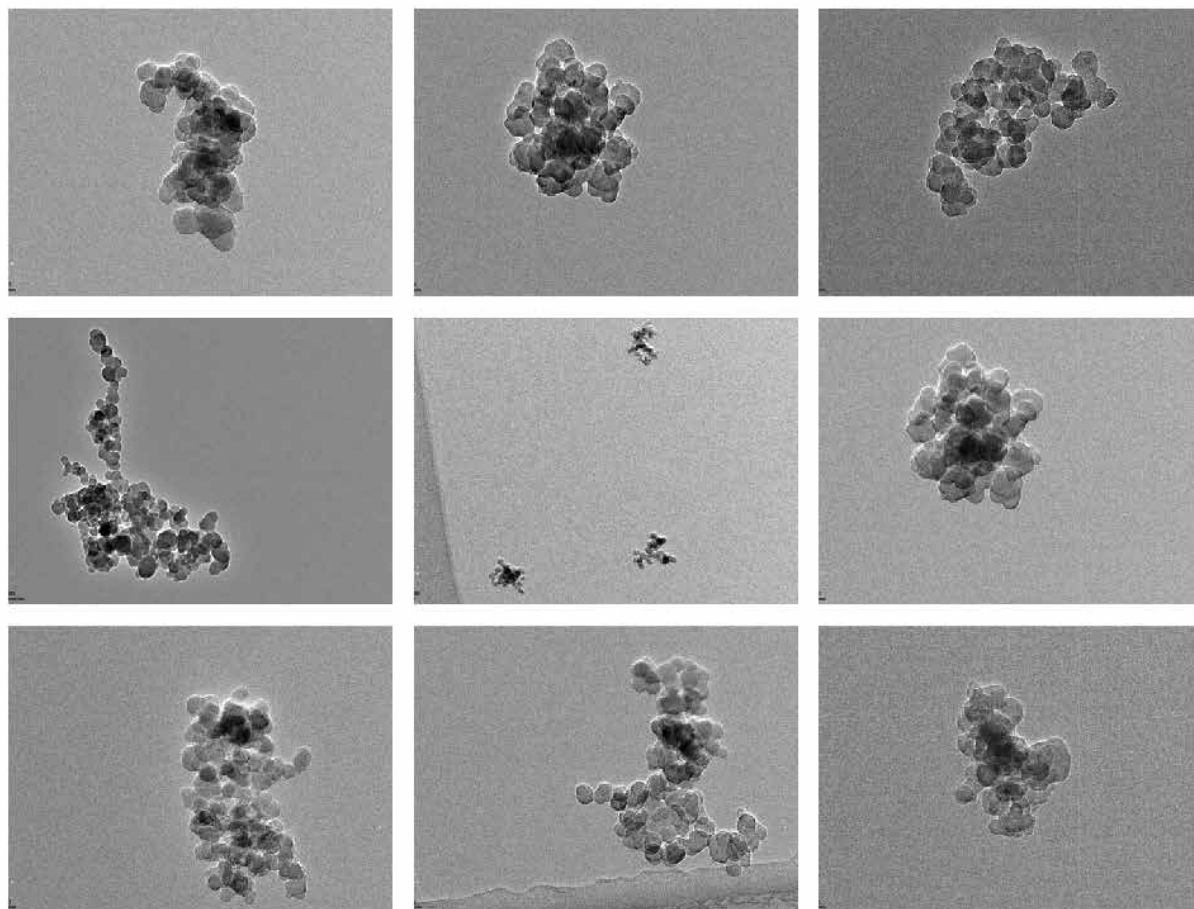
Figure S4. TEM images of 300 nm soot after anthracene coating ($m_1/m_0 = 2.6$) and denuding via Path **LS** of Figure **??**. Scale bars are omitted since all soot was composed of monomers with 30 nm diameter (Figure S8).

Figure S5. Data from Slowik *et al.* (2007), reanalyzed to illustrate coating/denuding without a change in the final d_{mob} or χ. Initial particle diameters are 135, 225, and 310 nm. This demonstrates deposition/sublimation of anthracene (Path **SS** in Figure **??**). Left and right panels show mobility diameter and shape factor χ as a function of coating volume. Circles reflect oleic acid condensation, squares anthracene deposition. Since $\chi \approx 1$ at large V_1/V_0 for both substances, anthracene likely condensed as a supercooled liquid. The fits on the right hand side reach a minimum of $\chi = 1.37$, 1.3, and 1.0 for the 310, 225, and 135 nm particles, respectively.

Figure S6. Photograph of a spatula upon which anthracene was deposited in our coating apparatus. The crystalline structure of the deposit is clearly visible. The conditions used for this experiment were used for the experiment labelled Path **SS** in Figure **??**.
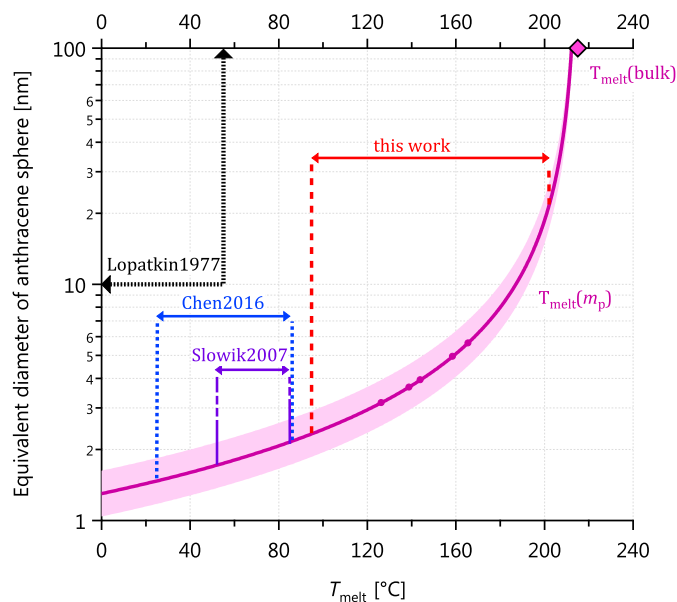
Figure S7. Melting point depression of nanoscopic quantities of anthracene, as discussed in the text. Overlaid are the temperatures at which these and related anthracene experiments have been carried out. The curve indicates the melting point depression for nanoscopic quantities of anthracene based on molecular dynamics simulations at the points marked with spheres (Chen *et al.*, 2014). The asymptote of this curve is the melting point of bulk anthracene (216 °C, ♦). The studies of Chen *et al.* (2016) and Slowik *et al.* (2007) are similar to ours and discussed in Section **??**; the study by (Lopatkin *et al.*, 1977) showed that anthracene thin films (thickness 10 nm to 16 μm) form as liquids below 55 °C.
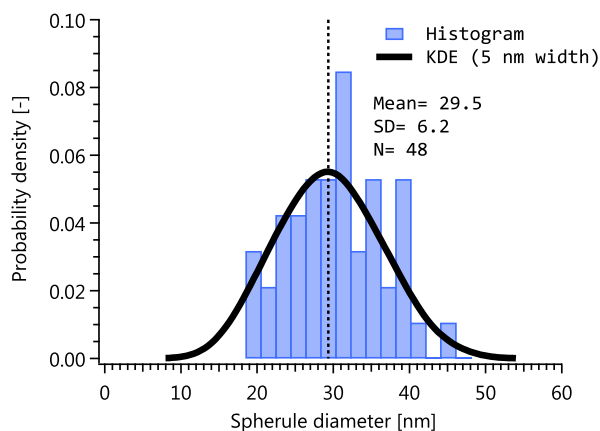
Figure S8. CAST Soot spherule diameters, measured manually from the TEM images. KDE is the kernel density estimated with a Gaussian kernel.

References

Aubin, D.G. and Abbatt, J.P., 2006. Laboratory measurements of thermodynamics of adsorption of small aromatic gases to n-hexane soot surfaces, *Environ. Sci. Technol.*, 40 (1), 179–187.

Burtscher, H., Baltensperger, U., Bukowiecki, N., Cohn, P., Hüglin, C., Mohr, M., Matter, U., Nyeki, S., Schmatloch, V., Streit, N., and Weingartner, E., 2001. Separation of volatile and non-volatile aerosol fractions by thermodesorption: instrumental development and applications, *J. Aerosol Sci.*, 32 (4), 427–442.

Chen, C., Enekwizu, O.Y., Fan, X., Dobrzanski, C.D., Ivanova, E.V., Ma, Y., Gor, G.Y., and Khalizov, A.F., 2018. Single parameter for predicting the morphology of atmospheric black carbon, *Environmental Science & Technology*, 52 (24), 14169–14179.

Chen, C., Fan, X., Shaltout, T., Qiu, C., Ma, Y., Goldman, A., and Khalizov, A.F., 2016. An unexpected restructuring of combustion soot aggregates by subnanometer coatings of polycyclic aromatic hydrocarbons, *Geophys. Res. Lett.*, 43 (20), 11080–11088.

Chen, D., Totton, T.S., Akroyd, J.W., Mosbach, S., and Kraft, M., 2014. Size-dependent melting of polycyclic aromatic hydrocarbon nano-clusters: A molecular dynamics study, *Carbon*, 67, 79–91.

Christenson, H.K., 2001. Confinement effects on freezing and melting, *Journal of Physics: Condensed Matter*, 13 (11), R95–R133.

DeCarlo, P., Slowik, J., Worsnop, D., Davidovits, P., and Jimenez, J., 2004. Particle morphology and density characterization by combined mobility and aerodynamic diameter measurements. part 1: Theory, *Aerosol Sci. Technol.*, 38, 1185–1205.

Ferry, D., Suzanne, J., Nitsche, S., Popovitcheva, O.B., and Shonija, N.K., 2002. Water adsorption and dynamics on kerosene soot under atmospheric conditions, *Journal of Geophysical Research: Atmospheres*, 107 (D23), AAC 22–1–AAC 22–10.

Ghazi, R. and Olfert, J., 2013. Coating mass dependence of soot aggregate restructuring due to coatings of oleic acid and dioctyl sebacate, *Aerosol Sci. Technol.*, 47 (2), 192–200.

Jennings, S.G., 1988. The mean free path in air, *J. Aerosol Sci.*, 19 (2), 159–166.

Laborde, M., Mertes, P., Zieger, P., Dommen, J., Baltensperger, U., and Gysel, M., 2012. Sensitivity of the single particle soot photometer to different black carbon types, *Atmos. Meas. Tech.*, 5, 1031–1043.

Lopatkin, Y.M., Protsenko, I.E., and Skorobogatko, A.F., 1977. Structure of anthracene thin films, *Krist. Tech.*, 12 (9), 903–905.

Ma, X., Zangmeister, C.D., Gigault, J., Mulholland, G.W., and Zachariah, M.R., 2013. Soot aggregate restructuring during water processing, *J. Aerosol Sci.*

Marcolli, C., 2014. Deposition nucleation viewed as homogeneous or immersion freezing in pores and cavities, *Atmos. Chem. Phys.*, 14 (4), 2071–2104.

Maricq, M.M., 2014. Examining the relationship between black carbon and soot in flames and engine exhaust, *Aerosol Sci. Technol.*, 48 (6), 620–629.

Moteki, N. and Kondo, Y., 2007. Effects of mixing state on black carbon measurements by laser-induced incandescence, *Aerosol Sci. Technol.*, 41 (4), 398–417.

Nanda, K.K., 2009. Size-dependent melting of nanoparticles: Hundred years of thermodynamic model, *Pramana - J Phys*, 72 (4), 617–628.

Nemes-Incze, P., Osváth, Z., Kamarás, K., and Biró, L., 2008. Anomalies in thickness measurements of graphene and few layer graphite crystals by tapping mode atomic force microscopy, *Carbon*, 46 (11), 1435–1442.

Nguyen, H.V., Okuyama, K., Mimura, T., Kousaka, Y., Flagan, R.C., and Seinfeld, J.H., 1987. Homogeneous and heterogeneous nucleation in a laminar flow aerosol generator, *Journal of Colloid and Interface Science*, 119 (2), 491–504.

Pawlow, P., 1909. Über die abhängigkeit des schmelzpunktes von der oberflächenenergie eines festen körpers, *Z. phys. Chem*, 65, 1–35.

Roux, M.V., Temprado, M., Chickos, J.S., and Nagano, Y., 2008. Critically evaluated thermochemical properties of polycyclic aromatic hydrocarbons, *Journal of Physical and Chemical Reference Data*, 37 (4), 1855–1996.

Schmidt, M., Kusche, R., von Issendorff, B., and Haberland, H., 1998. Irregular variations in the melting point of size-selected atomic clusters, *Nature*, 393 (6682), 238–240.

Schwarz, J.P., Gao, R.S., Fahey, D.W., Thomson, D.S., Watts, L.A., Wilson, J.C., Reeves, J.M., Darbeheshti, M., Baumgardner, D.G., Kok, G.L., Chung, S.H., Schulz, M., Hendricks, J., Lauer, A., Kärcher, B., Slowik, J.G., Rosenlof, K.H., Thompson, T.L., Langford, A.O., Loewenstein, M., and Aikin, K.C., 2006. Single-particle measurements of midlatitude black carbon and light-scattering aerosols from the boundary layer to the lower stratosphere, *J. Geophys. Res.*, 111, D16207.

Slowik, J.G., Cross, E.S., Han, J.H., Kolucki, J., Davidovits, P., Williams, L.R., Onasch, T.B., Jayne, J.T., Kolb, C.E., and Worsnop, D.R., 2007. Measurements of morphology changes of fractal soot particles using coating and denuding experiments: Implications for optical absorption and atmospheric lifetime, *Aerosol Sci. Technol.*, 41 (8), 734–750.

Tajima, N., Fukushima, N., Ehara, K., and Sakurai, H., 2011. Mass range and optimized operation of the aerosol particle mass analyzer, *Aerosol Sci. Technol.*, 45 (2), 196–214.